

# Radially Oriented Single-Crystal Primary Nanosheets Enable Ultrahigh Rate and Cycling Properties of $\text{LiNi}_{0.8}\text{Co}_{0.1}\text{Mn}_{0.1}\text{O}_2$ Cathode Material for Lithium-Ion Batteries

Xing Xu, Hua Huo, Jiyuan Jian, Liguang Wang, He Zhu, Sheng Xu, Xiaoshu He, Geping Yin, Chunyu Du,\* and Xueliang Sun\*

Ni-rich  $\text{Li}[\text{Ni}_x\text{Co}_y\text{Mn}_{1-x-y}]\text{O}_2$  ( $x \geq 0.8$ ) layered oxides are the most promising cathode materials for lithium-ion batteries due to their high reversible capacity of over  $200 \text{ mAh g}^{-1}$ . Unfortunately, the anisotropic properties associated with the  $\alpha\text{-NaFeO}_2$  structured crystal grains result in poor rate capability and insufficient cycle life. To address these issues, a micrometer-sized Ni-rich  $\text{LiNi}_{0.8}\text{Co}_{0.1}\text{Mn}_{0.1}\text{O}_2$  secondary cathode material consisting of radially aligned single-crystal primary particles is proposed and synthesized. Concomitant with this unique crystallographic texture, all the exposed surfaces are active  $\{010\}$  facets, and 3D  $\text{Li}^+$  ion diffusion channels penetrate straightforwardly from surface to center, remarkably improving the  $\text{Li}^+$  diffusion coefficient. Moreover, coordinated charge–discharge volume change upon cycling is achieved by the consistent crystal orientation, significantly alleviating the volume-change-induced intergrain stress. Accordingly, this material delivers superior reversible capacity ( $203.4 \text{ mAh g}^{-1}$  at 3.0–4.3 V) and rate capability ( $152.7 \text{ mAh g}^{-1}$  at a current density of  $1000 \text{ mA g}^{-1}$ ). Further, this structure demonstrates excellent cycling stability without any degradation after 300 cycles. The anisotropic morphology modulation provides a simple, efficient, and scalable way to boost the performance and applicability of Ni-rich layered oxide cathode materials.

3.8 V (vs  $\text{Li}^+/\text{Li}$ ), making them a class of promising cathode material and attracting considerable attention. Nevertheless, the inferior cycling stability and poor rate capability of Ni-rich oxide cathode materials have to be overcome before they can compete in practical implementation.<sup>[2,4]</sup> These drawbacks are largely attributed to their spherical micrometer-sized secondary particles aggregated densely by many randomly oriented primary nanoparticles,<sup>[4–6]</sup> as shown in Figure 1a. On the one hand, concomitant with this structure, the surface of secondary particles is terminated with random crystal planes. As  $\text{Li}^+$  can only diffuse along the 2D  $\{010\}$  plane in the hexagonal-layer structure of NCM materials,<sup>[4,7]</sup> the randomly exposed crystal planes (not solely the active  $\{010\}$  plane) may substantially hinder the  $\text{Li}^+$  exchange at the electrode/electrolyte interface. Meanwhile, the randomly oriented primary nanoparticles induce a prolonged and mazy  $\text{Li}^+$  diffusion pathway inside the secondary particles, because  $\text{Li}^+$  ions have to migrate across the grain boundaries, especially between the grains with incon-

sistent crystal planes. On the other hand, the successive phase transition accompanied by repeated  $\text{Li}^+$  insertion/extraction would result in anisotropic variation of the lattice parameters, and such variation is severely aggravated with the increase of Ni content.<sup>[8]</sup> Accordingly, in the Ni-rich oxide cathode materials, the substantial anisotropic lattice expansion/contraction would result in drastic microstrains at the boundaries of randomly oriented primary particles due to the asynchronous volume

## 1. Introduction

Advanced cathode materials with high specific capacity are in urgent need to meet the increasing demand for high energy density lithium-ion batteries.<sup>[1–3]</sup> Among numerous cathode candidates, Ni-rich  $\text{LiNi}_x\text{Co}_y\text{Mn}_{1-x-y}\text{O}_2$  (NCM) layered oxides, typically  $\text{LiNi}_{0.8}\text{Mn}_{0.1}\text{Co}_{0.1}\text{O}_2$ , can deliver a high capacity of above  $200 \text{ mAh g}^{-1}$  with an average discharge potential of

X. Xu, Prof. H. Huo, J. Jian, Dr. L. Wang, S. Xu, X. He,  
Prof. G. Yin, Prof. C. Du  
School of Chemistry and Chemical Engineering  
Harbin Institute of Technology  
Harbin 150001, China  
E-mail: cydu@hit.edu.cn

 The ORCID identification number(s) for the author(s) of this article can be found under <https://doi.org/10.1002/aenm.201803963>.

Dr. H. Zhu  
Department of Physics and Material Science  
City University of Hong Kong  
Hong Kong 999077, China  
Prof. X. Sun  
Department of Mechanical and Materials Engineering  
University of Western Ontario  
London, ON N6A 5 B9, Canada  
E-mail: xsun9@uwo.ca

DOI: 10.1002/aenm.201803963

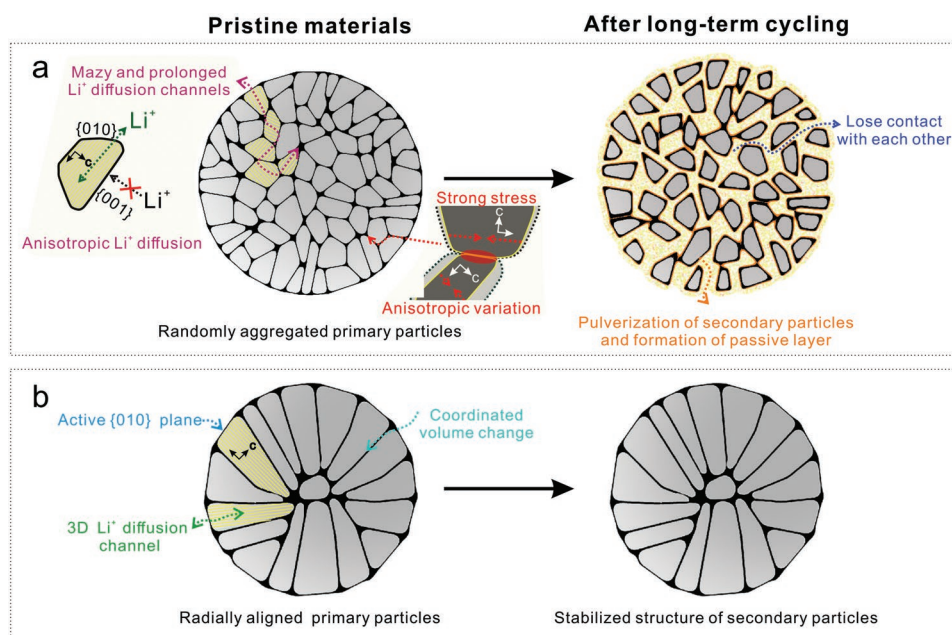


**Figure 1.** Schematic illustration of the structure and characteristics of a) C-NCM (commercial NCM) and b) RASC-NCM materials.

change. Consequently, cracks may develop and propagate along the grain boundaries until entire pulverization of secondary particles and even spalling off of primary particles, which has been identified as one of the main reasons for the rapid degradation of Ni-rich NCM materials upon long-term cycling.<sup>[9–13]</sup>

These issues concerning the hierarchical secondary particles of Ni-rich NCM materials cannot be effectively resolved by the conventional modification technologies of surface coating and lattice ion doping, because surface coating is mainly used to depress the side reactions between cathode and electrolyte,<sup>[14,15]</sup> while the lattice ion doping is usually intended to restrict the phase transitions during the charge–discharge processes.<sup>[13,16]</sup> In view of the high anisotropy in Li<sup>+</sup> diffusion<sup>[17,18]</sup> and lattice expansion/contraction<sup>[19,20]</sup> of hexagonal-layered NCM materials, morphological modulation will be an efficient way to enhance their rate capability and cycling stability.<sup>[4]</sup> However, structurally and morphologically controlled synthesis of NCM materials with superior rate and cycling properties remains a great challenge, in particular in a mass production manner.

Herein, we propose an advanced Ni-rich LiNi<sub>0.8</sub>Co<sub>0.1</sub>Mn<sub>0.1</sub>O<sub>2</sub> cathode material with radially aligned single-crystal primary particles (RASC-NCM) shown in Figure 1b, which is massively synthesized using a modified coprecipitation method followed by a solid-state reaction. With the radially oriented single-crystal primary particles penetrating from surface to center, all the exposed surface is the electrochemically active {010} planes, and Li<sup>+</sup> ions diffuse straightforwardly from center to surface without crossing grain boundaries, building up facilitated 3D Li<sup>+</sup> channels. Moreover, the radial primary particles with consistent crystal orientation might significantly alleviate the volume-change-induced intergrain stress by coordinated expansion and contraction, which can remarkably depress the pulverization of secondary particles and promote the cycling stability. In accordance with this unique structure, superior reversible capacity (203.4 mAh g<sup>-1</sup> at 0.1C rate) and rate capability

(152.7 mAh g<sup>-1</sup> at 5C rate) are obtained. More importantly, the RASC-NCM material is extremely stable without any visible degradation after 300 charge–discharge cycles. Our work provides an efficient and up-scalable strategy for enhancing the rate and cycling properties of Ni-rich NCM materials, making them a rather promising cathode candidate for lithium-ion batteries.

## 2. Results and Discussions

Morphologies of the RASC-NCM material and its corresponding hydroxide precursor are characterized by scanning electron microscope (SEM) as shown in Figure 2. The RASC-NCM precursor displays a good spherical morphology with nearly monodispersed size distribution (Figure 2a). The high-magnification SEM image (Figure 2b) clearly illustrates that the micrometer-sized secondary particle is assembled by densely aggregated primary particles. Moreover, compared with the C-NCM precursor with much smaller irregular primary nanoparticles (Figure S1, Supporting Information), these primary particles are in the form of self-assembled multilayer nanosheets with an orderly arrangement. Average thickness of each single-layer nanosheet is about 50 nm, and the length of the exposed lateral dimension is 300–1000 nm. From the cross-sectional SEM image in Figure 2c, we can observe that all the multilayer nanosheets are embedded into the spherical secondary particle along the radial direction, continuously from the center to the surface. Morphology of the precursor collected at different reaction times during the coprecipitation process is presented in Figure S2 (Supporting Information). It can be found that the thin flaky primary particles assemble into flower-like secondary particles. With time, the secondary particles grow gradually and become more uniform and denser as the primary particles evolve from monolayer at 10 h to multilayer at 30 h, reducing the voids between primary particles. Moreover,

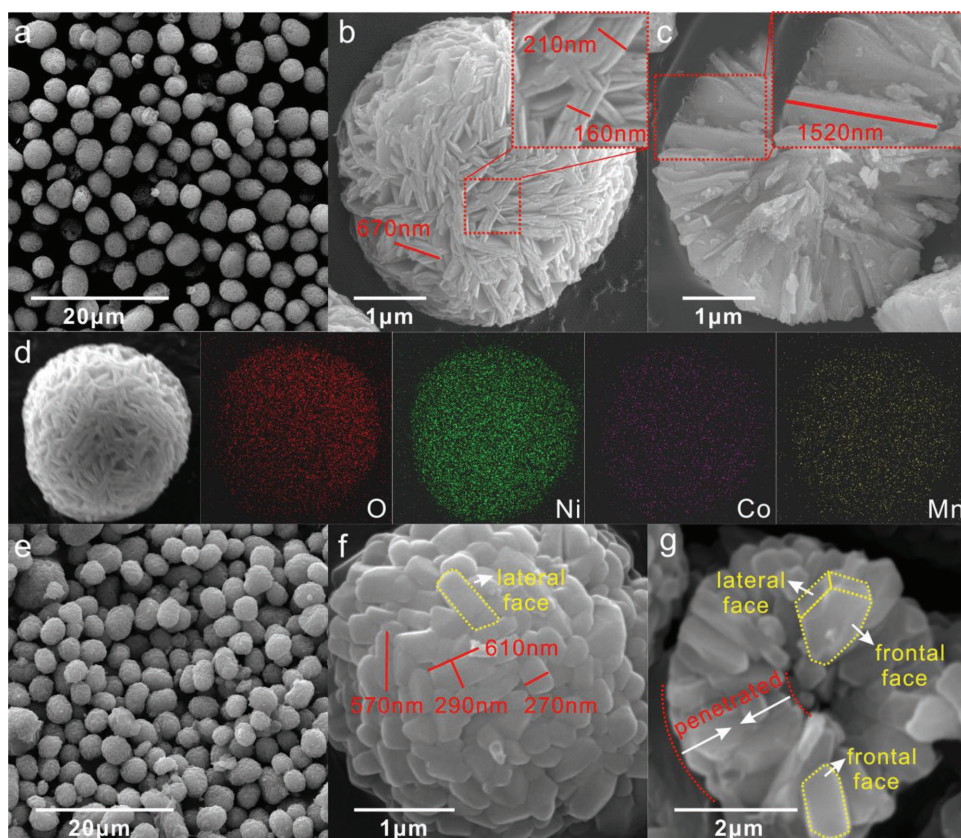


**Figure 2.** a–c) SEM and cross-sectional SEM images of RASC-NCM precursor; d) EDS elemental mapping of RASC-NCM precursor; e–g) SEM and cross-sectional SEM images of RASC-NCM.

the high-magnification SEM images reveal that the nanosheets are all embedded into the secondary particles preferentially along the radial direction, which might be due to the selectively electrostatic absorption of a large amount of  $\text{NH}_4^+$  as surfactant on the (001) plane during the synthesis process.<sup>[21]</sup> The energy-dispersive X-ray spectroscopy (EDS) elemental mapping in Figure 2d illustrates the homogeneous distribution of Ni, Co, and Mn elements throughout the precursor particle, confirming the complete coprecipitation process.

After the lithiation reaction at high temperature, the spherical morphology and size of the RASC-NCM secondary particles are maintained (Figure 2e–g) compared with the precursor (Figure 2a–c). Nevertheless, the morphology of the primary particles changes substantially. The thickness of RASC-NCM primary particles increases greatly to about 200–300 nm, which should be due to the mergence of the multilayered nanosheets with each other during the high-temperature calcination. Noteworthy is that the radial orientation of the nanosheets in the precursor is retained as shown by the cross-sectional SEM image in Figure 2g. Moreover, the secondary particle is mainly composed of radial single-crystal nanosheets penetrated continuously from the center to the surface, with their frontal faces tightly adhered to each other and their lateral faces directed to the surface of the spherical secondary particles.

The nanosheets of RASC-NCM material are investigated by transmission electron microscopy (TEM), as shown in Figure 3.

The high-resolution TEM (HRTEM) image (Figure 3b) taken from the frontal plane of the nanosheet (Figure 3a) displays two sets of clear lattice fringes with the same interplanar distance of 2.46 Å at an angle of  $120^\circ$ , corresponding to the (0 $\bar{1}$ 0) and (100) planes of the RASC-NCM material, respectively. The interplanar distance of 4.75 Å (Figure 3e), taken from one lateral plane of the nanosheet (Figure 3d), is assigned to the (003) plane. Combined with the corresponding selected area electron diffraction (SAED) patterns (Figure 3c,f), we confirm that the nanosheets are single crystals with a hexagonal layered structure capped by {001} planes and the electrochemically active {010} planes located at the lateral direction. As illustrated in Figure 3g, the {001} planes containing (001) and (00 $\bar{1}$ ) facets are perpendicular to *c*-axis, while the {010} planes, including (010), (0 $\bar{1}$ 0), (100), (110), (1 $\bar{1}$ 0), and ( $\bar{1}$ 00) facets, are parallel to *c*-axis and provide 2D  $\text{Li}^+$  diffusion channels. Thus, we can conclude that the spherical RASC-NCM secondary particles are assembled by radially aligned single-crystal nanosheets, with the {001} planes closely adhered to each other and the electrochemically active {010} planes orderly exposed to the surface. This unique crystallographic texture of the primary particles along the radial direction establishes a facilitated 3D  $\text{Li}^+$  diffusion channel straightforwardly from center to surface of secondary particles, thereby increasing the  $\text{Li}^+$  diffusion coefficients and rate capability of the NCM cathode materials. At the same time, the radial oriented primary particles with coherent {001} crystal facets can alleviate the intergrain stress

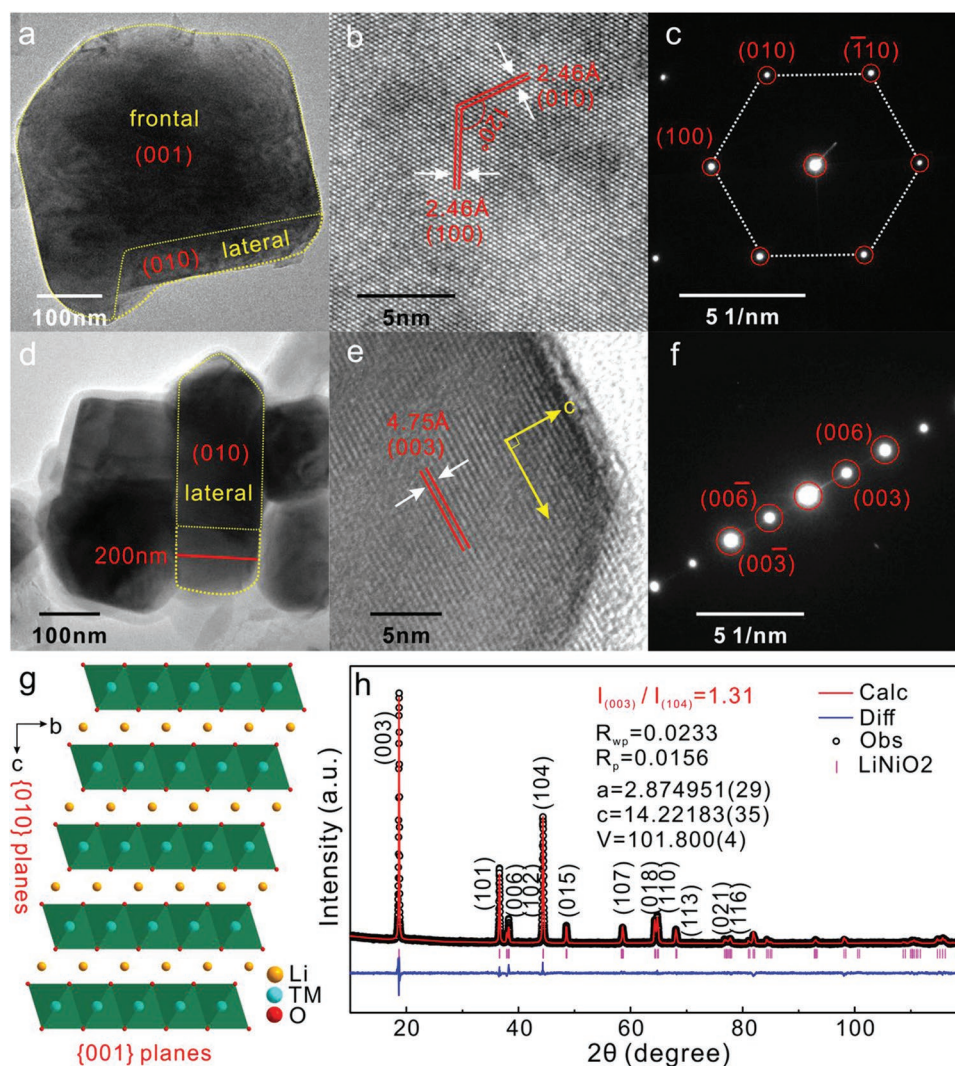


**Figure 3.** a–c) TEM, HRTEM images and SAED pattern from the frontal plane of the RASC-NCM nanosheet; d–f) TEM, HRTEM images and SAED pattern from the lateral plane of the RASC-NCM nanosheet; g) Crystal structure of NCM material; h) Refined XRD pattern and results of RASC-NCM material based on  $\text{LiNiO}_2$  hexagonal (R-3m) phase.

induced by their volume expansion and contraction during  $\text{Li}^+$  intercalation/deintercalation, stabilizing the hierarchical structure of the secondary RASC-NCM particles.

However, for the C-NCM cathode (Figure S1f, Supporting Information), the secondary particles are aggregated by irregularly shaped and randomly oriented primary particles with much smaller size. This indicates that there must be multiple separate primary particles from the surface to the center of the secondary particles, and their surface is terminated with random crystal planes, which hinder the  $\text{Li}^+$  exchange at the electrode/electrolyte interface and limit  $\text{Li}^+$  diffusivity inside the secondary particles. Meanwhile, the uncooperative expansion/contraction of the crystal volume of randomly oriented primary particles results in large local microstrain between them, deteriorating the long-term cycling stability. These distinctive features between the two cathode materials can be further distinguished in Figure S3 (Supporting Information).

The powder X-ray diffraction (XRD) pattern of RASC-NCM is collected and refined as depicted in Figure 3h, which exhibits well-developed hexagonal  $\alpha\text{-NaFeO}_2$  structure with R-3m symmetry without impurity phase. The  $I_{(003)}/I_{(104)}$  intensity ratio of RASC-NCM, which is usually used to reflect the degree of cation mixing, is 1.31, which is higher than that of C-NCM (Figure S4, Supporting Information), indicating a negligible  $\text{Li}^+/\text{Ni}^{2+}$  cation mixing.<sup>[22]</sup> Moreover, by the Rietveld refinement, slightly smaller lattice parameters  $a$  and  $c$  are obtained for RASC-NCM compared with C-NCM (Figure S4, Supporting Information). These results indicate a better crystallinity of RASC-NCM material, which might be attributed to the radially aligned primary particles, facilitating the reaction between the precursor and lithium source during the high-temperature calcination process.

Electrochemical performance of RASC-NCM is tested to investigate the function of its unique morphology in comparison with C-NCM material using 2025 coin-type cells in the

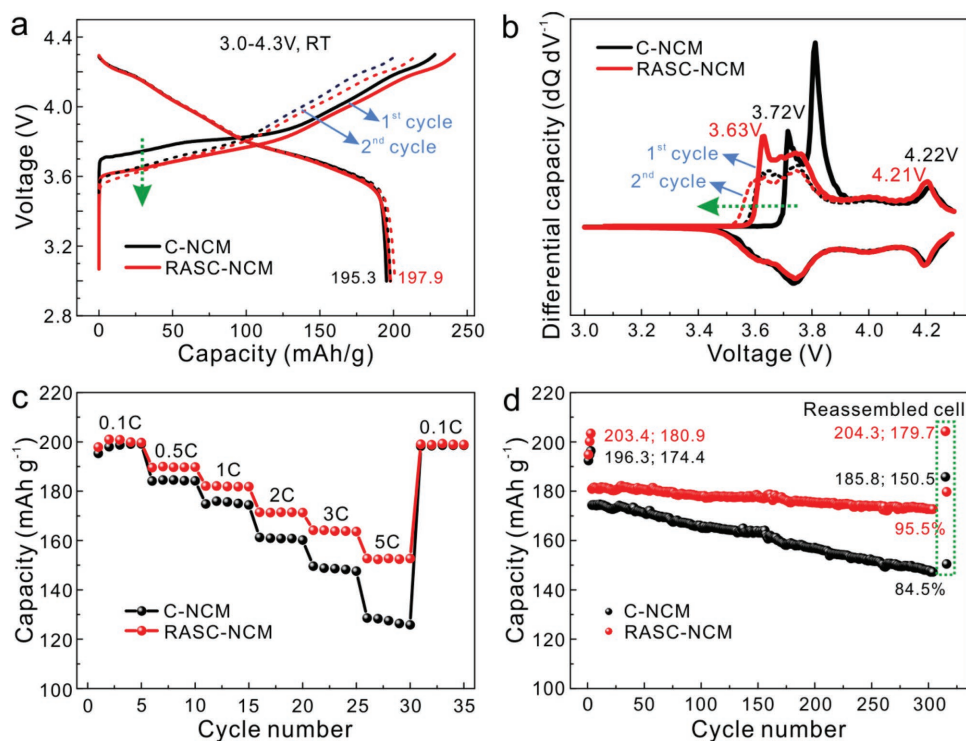


**Figure 4.** Electrochemical performances of C-NCM and RASC-NCM cells at 3.0–4.3 V and 25 °C: a) The charge–discharge curves for the first and second cycles at 0.1C rate; b) Differential capacity curves of the first and second charge–discharge cycles; c) Rate capability at various charge and discharge rates; d) Cycling performances at 1C rate.

voltage range between 3.0 and 4.3 V (vs Li<sup>+</sup>/Li). **Figure 4a** shows the charge–discharge curves of the two cells for the first two cycles at the current rate of 0.1C (20 mA g<sup>-1</sup>). Both RASC-NCM and C-NCM cells exhibit smooth charge–discharge features and deliver a high initial discharge capacity of 197.9 and 195.3 mAh g<sup>-1</sup>, respectively. However, a strikingly decreased charging voltage of ≈90 mV at the first cycle and ≈35 mV at the second cycle can be observed for the RASC-NCM cathode in comparison with the C-NCM one, as indicated by the arrow. This means that the Li<sup>+</sup> deintercalation in the RASC-NCM material is more facilitated.

To further reveal the different charge–discharge behaviors of the two cells, their corresponding differential capacity (dQ/dV) profiles as a function of cell voltage are shown in **Figure 4b**. These curves are mainly characterized by three couples of redox peaks, which are attributed to the biphasic regions with the structural transition from hexagonal to monoclinic (H1 to M), monoclinic to hexagonal (M to H2), and hexagonal to hexagonal (H2 to H3) during the Li<sup>+</sup> extraction/insertion processes.<sup>[23,24]</sup> In accordance with the charge–discharge curves, much lower anodic peak voltages in differential capacity curves are observed for the RASC-NCM electrode during the charging process for the initial cycles. Besides, the voltage interval between the anodic and corresponding cathodic peaks of RASC-NCM is also substantially smaller than that of the C-NCM. These results demonstrate greatly decreased polarization, which can be attributed to its unique morphology. In contrast to the C-NCM cathode, whose randomly oriented primary particles induce mazy and prolonged Li<sup>+</sup> diffusion and

electron transfer channels, the radially oriented single-crystal primary particles with the active {010} facets exposed to the electrolyte would provide a straightforward 3D Li<sup>+</sup> transport and electron transfer channels from surface to center of the secondary particles. This conclusion is confirmed by the considerably enhanced Li<sup>+</sup> diffusion coefficient and electronic conductivity of RASC-NCM cathode obtained by the potentiostatic intermittent titration technique (PITT) and four-point probe volt-ampere methods, which are about two and ten times higher than those of C-NCM, respectively (**Figure S5** and **Table S1**, Supporting Information). This simultaneously increased Li<sup>+</sup> diffusion and electron transfer substantially decrease the polarization of RASC-NCM cathode, ensuring a much better electrochemical performance of RASC-NCM material.

The rate capabilities at different current densities ranging from 20 to 1000 mA g<sup>-1</sup> (0.1 to 5C) are displayed in **Figure 4c**. Although the RASC-NCM electrode exhibits only slightly higher discharge capacity at 0.1C rate than the C-NCM one, the capacity difference becomes much more apparent when increasing the current density. Even at 5C rate (1000 mA g<sup>-1</sup>), the RASC-NCM electrode can still deliver a high discharge capacity of 152.7 mAh g<sup>-1</sup> (77.2% of the capacity at 0.1C), which is much higher than 128.6 mAh g<sup>-1</sup> of the C-NCM (65.8% of the capacity at 0.1C). Such a discharge capacity at 5C rate is among the highest values reported in literature (**Figure S6**, Supporting Information), which is much beneficial to the fast charge/discharge applications.

To reveal the major reasons for the superior rate capability of RASC-NCM cathode, the corresponding differential

capacity profiles at different current densities are displayed in Figure S7 (Supporting Information). As the C-rate increases, both the onset and the peak voltages of the anodic peaks during the charging process move positively, and only partial anodic peaks at 3.7 and 4.2 V can be observed at high C-rates. Correspondingly, the cathodic peaks show a continuous decrease in intensity and voltage. These polarization behaviors are especially severe for C-NCM. Its anodic peak at 4.2 V disappears completely when the applied current density is above 3C rate, because the large polarization shifts it to beyond the cutoff voltage of 4.3 V, and the corresponding cathodic peak is also missing. In comparison, the polarization is notably depressed for the RASC-NCM. Even at 5C rate, the redox peaks at 4.2 V are still distinguishable. The depressed polarization should be ascribed to the unique structure of radially oriented single-crystal primary particles of RASC-NCM secondary particles, as discussed above, which endows both high  $\text{Li}^+$  diffusivity and electronic conductivity to the NCM materials.

Figure 4d shows the representative cycling performance of the two cells at the current rate of 1C after the activation at 0.1C rate for three cycles (reproducible data are shown in Figure S8, Supporting Information). After the activation, the discharge capacities of RASC-NCM electrode are  $203.4 \text{ mAh g}^{-1}$  at 0.1C and  $180.9 \text{ mAh g}^{-1}$  at 1C, which are higher than those of C-NCM ( $196.3 \text{ mAh g}^{-1}$  at 0.1C and  $174.4 \text{ mAh g}^{-1}$  at 1C). Moreover, apart from higher initial capacity, the RASC-NCM cell delivers a rather stable cyclability, and up to 95.5% ( $172.7 \text{ mAh g}^{-1}$ ) of its initial capacity remains after 300 cycles.

By contrast, the C-NCM cell shows much inferior capacity retention of only 84.5% ( $147.3 \text{ mAh g}^{-1}$ ) during the same cycling period, although the specific surface area of C-NCM material ( $0.58 \text{ m}^2 \text{ g}^{-1}$ ) is somewhat lower than that of RASC-NCM ( $0.72 \text{ m}^2 \text{ g}^{-1}$ ) as demonstrated by Figure S9 (Supporting Information) (specific surface area of RASC-NCM precursor ( $9.64 \text{ m}^2 \text{ g}^{-1}$ ) is higher than that of C-NCM ( $5.98 \text{ m}^2 \text{ g}^{-1}$ ), which may be due to the aggregated larger primary particles induced voids inside secondary particles). To exclude the effect induced by the anode and electrolyte, we reassemble the cycled cells by replacing fresh Li metal anode and electrolyte. It is surprising that the RASC-NCM cathode almost completely recovers to its initial performance with a capacity of  $204.3 \text{ mAh g}^{-1}$  at 0.1C and  $179.7 \text{ mAh g}^{-1}$  at 1C rate. This indicates that the RASC-NCM material is extremely stable, and the degradation of RASC-NCM cell during the cycling is mainly attributed to the anode and the electrolyte. However, for the C-NCM cell, its initial performance is only partially recovered after renewing the anode and electrolyte, demonstrating the substantial structure decay of the C-NCM material.

The differential capacity curves during the cycling process are also employed to explore the origin of different cycling behaviors of the two cells (Figure 5). A rapid increase in polarization (the anodic and cathodic peaks continuously drift apart) and decrease in peak intensities are observed for the C-NCM cell during cycling. In particular, the anodic peak at 4.2 V gradually shifts out of the voltage window and the corresponding cathodic peak gradually decreases in intensity and almost disappears ultimately upon cycling. Meanwhile, accompanied by the right

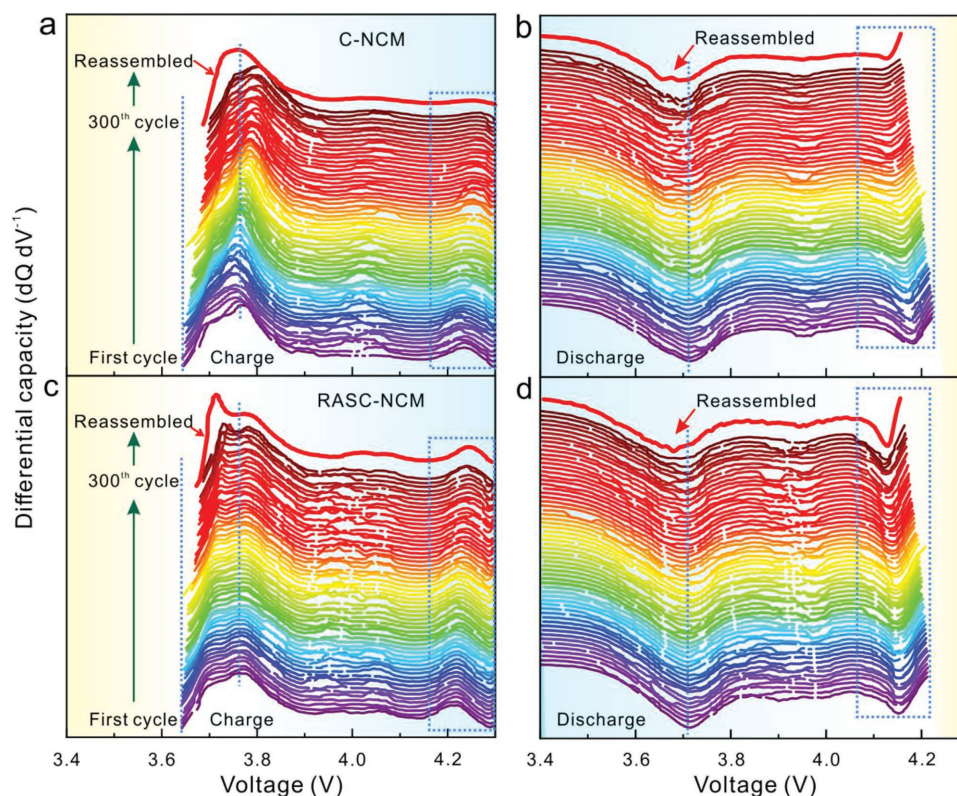


**Figure 5.** Differential capacity curves of a,b) C-NCM and c,d) RASC-NCM obtained from the charge–discharge curves every five cycles during the cycling tests.

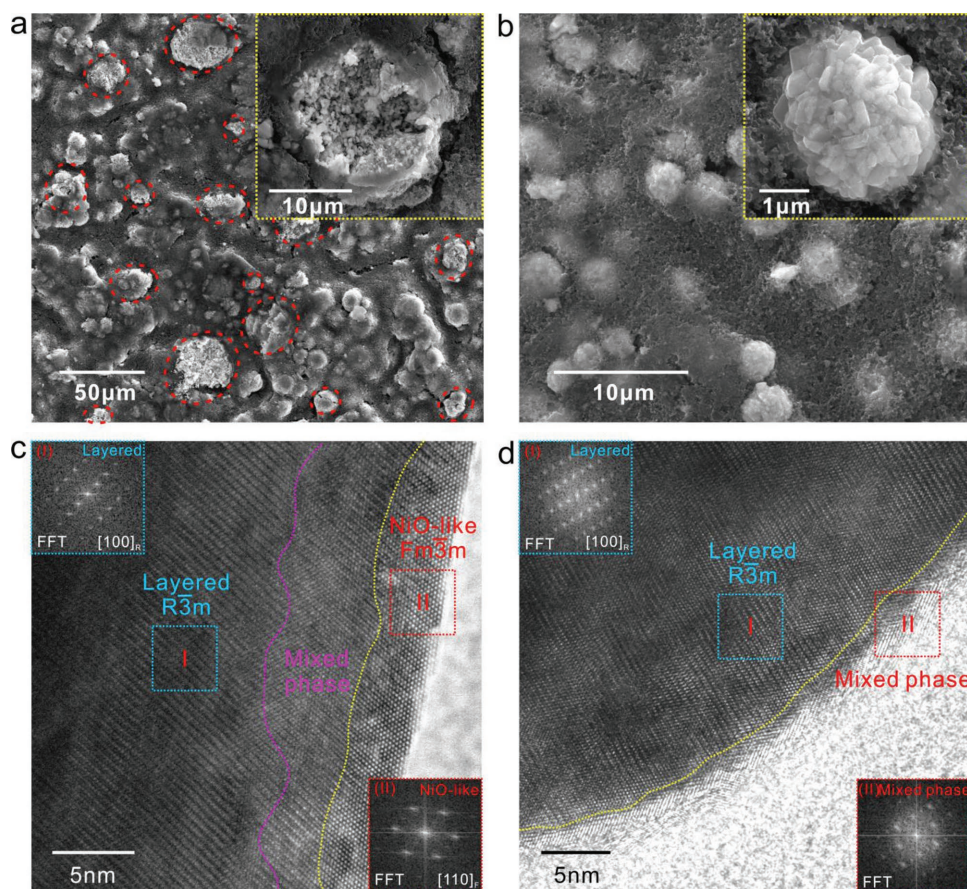


**Figure 6.** SEM images of the a) C-NCM and b) RASC-NCM cathodes after 300 cycles. Pulverized particles of C-NCM are marked with circles; HRTEM and the corresponding FFT patterns of the c) C-NCM and d) RASC-NCM cathodes after 300 cycles.

shift of the anodic peaks at 3.7 V, the onset charging voltage also gradually increases, which would partially submerge the anodic peak at 3.7 V and contribute to the intensity decrease of corresponding cathodic peak. These polarization behaviors lead to the fast capacity decay of C-NCM cell, which cannot be recovered even after reassembling the cell. In contrast, the polarization of RASC-NCM cell is significantly depressed. Even after 300 cycles, the anodic and cathodic peaks at high voltages are still distinctive and complete. Furthermore, the differential capacity curves of RASC-NCM cell almost completely regain its original profiles after renewing the anode and the electrolyte, despite a slightly larger polarization than the first cycle is observed probably due to the side reactions at the electrode/electrolyte interface. The average polarization voltage, the difference between average charge voltage and average discharge voltage, upon cycling is obtained. As shown in Figure S10 (Supporting Information), despite the similar values at the initial stage of the cycling, the average polarization voltage of RASC-NCM cell increases more slowly than that of C-NCM one, and their difference is gradually expanded to 34 mV after 300 cycles. This result clearly confirms the better stability of RASC-NCM material.

Previous studies have identified that the fragmentation of secondary particles of Ni-rich NCM materials is mainly responsible for the capacity degradation during cycling,<sup>[25]</sup> which is induced by the lattice volume expansion/contraction upon Li<sup>+</sup> ion extraction/reinsertion. Thus, the electrodes after long-term

cycling are disassembled and measured by SEM and TEM to analyze their structural and morphological degradation over cycling, as shown in Figure 6. After 300 cycles, severe pulverization of the secondary particles and spalling-off of the primary particles can be clearly observed for the C-NCM electrode, as indicated by circles and the magnified particle in the inset (Figure 6a). This is believed to originate from the intense strain generated by anisotropic lattice change accompanied by the repeated insertion/extraction of Li<sup>+</sup> ions (lattice parameters *a* and *c* change  $\approx 0.058$  and  $0.437$  Å for LiNi<sub>0.8</sub>Co<sub>0.1</sub>Mn<sub>0.1</sub>O<sub>2</sub>,<sup>[8]</sup> respectively). The anisotropic lattice variation would induce drastic microstrain at the asynchronous grain boundaries of randomly oriented primary C-NCM particles, and cracks may develop and propagate along the grain boundaries until entire pulverization of the secondary particles. Thus, some of the primary particles would lose electric contact with each other and do not participate in the electrochemical reaction any more. Meanwhile, electrolyte would infiltrate inside along the grain boundaries and its side reactions at the electrode/electrolyte interface would reduce Ni<sup>4+</sup> to Ni<sup>2+</sup>. The Ni<sup>2+</sup> ions are prone to migrating from the transition metal slabs to lithium ones, due to the similar ionic radius of Ni<sup>2+</sup> (0.69 Å) with that of Li<sup>+</sup> (0.76 Å), leading to the structure degradation at the particle surface.<sup>[13,26]</sup> This can be verified by the post-cycling TEM analysis shown in Figure 6 and Figure S11 (Supporting Information). Representatively, the high-resolution TEM image in Figure 6c taken from

the edge region of a cycled C-NCM particle reveals an uneven 3–5 nm NiO-like layer at the outmost surface, as illustrated by the fast Fourier transform (FFT) pattern (inset of Figure 6c). Below the NiO-like surface layer, a mixed phase layer of 3–6 nm can also be distinguished. Such passive surface layers have been reported to substantially inhibit Li<sup>+</sup> transportation and rapidly increase the impedance.<sup>[12,27]</sup> These factors contribute to the fast capacity decline as supported by the differential capacity curves during the cycling process (Figure 5).

In contrast, the RASC-NCM cathode shown in Figure 6b remains mechanically intact after the same period of cycling, and any fragmentation of spherical secondary particles can hardly be observed. Formation of cracks is inhibited by the unique crystallographic texture of radially aligned single-crystal primary particles, despite the fixed anisotropic lattice variation accompanied by the Li<sup>+</sup> insertion/extraction. These primary particles are tightly aggregated to each other with the identical {001} crystal facets, so that they would expand and contract at a coordinated pace during the charge–discharge process, effectively alleviating the microstrain at the grain boundaries. This improved mechanical stabilization prevents the infiltration of electrolyte and the formation of damaged surface layers. Thus, only few surfaces with 2–3 nm mixed phase layer can be observed on the surficial {010} facets of RASC-NCM particle, as demonstrated by the post-cycling TEM images in Figure 6d and Figure S11 (Supporting Information). Besides, the enhanced Li<sup>+</sup> diffusion coefficient and electronic conductivity of RASC-NCM material are beneficial to homogenizing the state of charge (SOC) on the particle level,<sup>[28,29]</sup> reducing the possibility of over delithiation at the particle surface. As a result, the unique RASC-NCM cell exhibits substantially improved cycling stability as shown in Figure 4d.

Meanwhile, side reactions at the electrode/electrolyte interface would also lead to formation of solid electrolyte interphase (SEI) film;<sup>[2,30]</sup> this can be confirmed by the SEM in combination with the EDS elemental analysis (Figure S12, Supporting Information) and the C1s X-ray photoelectron spectroscopy (XPS) surficial measurement<sup>[31,32]</sup> (Figure S13, Supporting Information) of the cycled electrodes. The similar surficial composition of the electrodes indicates comparable SEI films are determined at the surface of the two electrodes. Electrochemical impedance spectroscopy (EIS) measured at the charged state (4.3 V) before and after the extended cycles (Figure S14, Supporting Information) provides further support for the higher structural stability of RASC-NCM material. The semicircles in the high and medium frequencies are associated with the Li<sup>+</sup> diffusion across the surface film and the charge transfer resistance, respectively, while the oblique line at low frequency mainly reflects the Li<sup>+</sup> diffusion within the particles.<sup>[33]</sup> The fitted results by the equivalent circuit in Table S2 (Supporting Information) show that both the surface film resistance ( $R_{sf}$ ) and the charge transfer resistance ( $R_{ct}$ ) of RASC-NCM cell are markedly lower than those of C-NCM cell after the extended cycling. Especially, the charge transfer resistance of RASC-NCM cell is 128.1  $\Omega$ , while that of C-NCM cell drastically increases to 255.2  $\Omega$ . This result agrees well with the SEM and TEM images in Figure 6, indicating that the RASC-NCM material can retain well the unique radial structure of secondary particles, which would substantially restrain the impedance raise upon cycling.

### 3. Conclusions

In summary, by crystal anisotropy directed morphological modulation, the Ni-rich LiNi<sub>0.8</sub>Co<sub>0.1</sub>Mn<sub>0.1</sub>O<sub>2</sub> micrometer-sized secondary particles consisting of radially aligned single-crystal primary particles are massively prepared by a modified coprecipitation method followed with a solid-state reaction. Benefiting from the radially aligned single-crystal primary particles, the exposed active {010} plane and penetrated 3D Li<sup>+</sup> ion diffusion channels from surface to center are combined to ensure markedly improved Li<sup>+</sup> diffusivity. Simultaneously, the radially aligned primary particles with compatible crystal orientation lead to the coordinated volume changes upon cycling and thus extremely stable cyclability. As revealed by detailed electrochemical and structural analyses, the intergrain stress and the pulverization of the secondary particles have significant impact on the cycling stability. This work provides a promising strategy for tackling the rate and cycling problems, promoting the practical application of the Ni-rich NCM cathode materials.

### 4. Experimental Section

**Synthesis of RASC-NCM Material:** Precursor of RASC-NCM with a homogeneous composition of [Ni<sub>0.8</sub>Co<sub>0.1</sub>Mn<sub>0.1</sub>](OH)<sub>2</sub> was prepared by a modified coprecipitation method. To tune the morphology of the precursor, an optimized higher concentration of NH<sub>3</sub>·H<sub>2</sub>O and stirring speed were used, which were also proved to have significant impact on the coprecipitation process.<sup>[4,21]</sup> The optimized high NH<sub>3</sub>·H<sub>2</sub>O concentration (0.8 mol L<sup>-1</sup>) in the reactor can tune the growth direction and promote the growth of primary particles. The high stirring speed (the outer edge speed of impeller is 6.3 m s<sup>-1</sup>) can provide a strong mechanical agitation and uniform reaction environment, which prevents the nucleation and further reagglomeration of small secondary particles. Typically, an aqueous solution of CoSO<sub>4</sub>·7H<sub>2</sub>O, NiSO<sub>4</sub>·6H<sub>2</sub>O, and MnSO<sub>4</sub>·5H<sub>2</sub>O (2 mol L<sup>-1</sup>) with molar ratio of Ni:Co:Mn = 8:1:1 was pumped into a continuously stirred tank reactor (CSTR, 250 L) under N<sub>2</sub> atmosphere. Simultaneously, appropriate amount of NaOH solution (2 mol L<sup>-1</sup>, used as the precipitation agent and controlled by the pH meter) and NH<sub>3</sub>·H<sub>2</sub>O solution (4 mol L<sup>-1</sup>, used as chelating agent) was fed into the reactor separately. The temperature (60 °C), pH value (11.2), and stirring speed (300 rpm) of the solution were carefully controlled and maintained constant. Then, the precursor powders (about 100 kg per batch) were obtained through washing, filtering, and drying in a vacuum oven for 6 h to remove adsorbed water. LiNi<sub>0.8</sub>Co<sub>0.1</sub>Mn<sub>0.1</sub>O<sub>2</sub> cathode (RASC-NCM) material was prepared by a high-temperature sintering method. Initially, this precursor was thoroughly mixed with LiOH·H<sub>2</sub>O (Li:M ratio = 1.05:1), and excess lithium was used for the compensation of lithium loss during the sintering process. After that, the mixture was preliminarily annealed at 500 °C for 5 h, and subsequently calcined at 740 °C for 10 h in oxygen. For comparison, commercial LiNi<sub>0.8</sub>Co<sub>0.1</sub>Mn<sub>0.1</sub>O<sub>2</sub> (C-NCM) and its precursor were obtained from Ningbo Jinhe New Materials Co., Ltd., China.

**Materials Characterizations:** Crystalline structure of the samples was determined using a Panalytical Empyrean powder X-ray diffractometer with a Cu-K $\alpha$  radiation source ( $\lambda = 1.5481 \text{ \AA}$ , 45 kV, 50.0 mA). The Bragg angle was scanned over a range of 10°–120° at a scan rate of 4° min<sup>-1</sup>. The collected intensity data of XRD were analyzed by the Rietveld refinement program-General Structure Analysis System (GASA) software package. Morphology and elemental distribution of the samples were characterized by Helios Nanolab 600i high-resolution field emission scanning electron microscope (FESEM) equipped with an EDS analyzer with an acceleration voltage of 20 kV. HRTEM images were taken with a TecnaiG2F30 transmission electron microscope. The electronic conductivity of the samples was measured by a four-point probe

volt-ampere method (SANFENG SB 118). The Brunauer–Emmett–Teller (BET) surface area was obtained by N<sub>2</sub> adsorption/desorption isotherms at 77 K using a Bei Shi De 3H-2000PS1 instrument. XPS was conducted on a PHI model 5700 instrument with the Al K $\alpha$  source to analyze surface chemistry of the cycled electrodes.

**Electrochemical Measurements:** Electrochemical tests were carried out using the standard CR2025 coin-type cells. These cells were assembled in an Ar-filled glove box with the working cathode, Li metal anode, 1.0 M LiPF<sub>6</sub> in ethylene carbonate (EC)/dimethyl carbonate (DMC) (1:1 in volume) electrolyte, and polypropylene separators. To fabricate the cathodes, the active materials were thoroughly mixed with super-P carbon and polyvinylidene fluoride (8:1:1 in weight) in N-methylpyrrolidinon. The slurry thus obtained was spread onto an Al foil with a fixed thickness of 110  $\mu$ m and dried in a vacuum oven at 120 °C for 10 h. The Al foil coated by active materials was punched to circular disks. The mass loading of active materials was controlled within the range of 2–2.3 mg cm<sup>-2</sup>. Galvanostatic charge–discharge cycling of the cells was performed under the cutoff voltages of 3.0–4.3 V (vs Li<sup>+</sup>/Li). EIS was measured by an electrochemical workstation (PARSTAT 2273) with an amplitude of 10 mV and a frequency range from 10 mHz to 100 kHz. PITT measurement was conducted by applying a series of potential from 3.7 to 4.3 V with a step of 25 mV and recording the current after the current was less than 0.01C in each step. The Li<sup>+</sup> diffusion coefficient,  $\bar{D}$  (cm<sup>2</sup> s<sup>-1</sup>), was calculated from the following equation

$$\bar{D} = -\frac{d \ln(I) 4L^2}{dt \pi^2} \quad (1)$$

where  $I(t)$  is the transient current (mA),  $t$  the time (s),  $\pi$  the constant, and  $L$  the thickness of the electrodes (cm).<sup>[34]</sup>

## Supporting Information

Supporting Information is available from the Wiley Online Library or from the author.

## Acknowledgements

X.X. and H.H. contributed equally to this work. This work was financially supported by the National Key R&D Program of China (No. 2016YFB0100200), Applied Technology Research and Development Program of Harbin (Grant No. 2013DB4AP030), and National Natural Science Foundation of China (Grant No. 21673065).

## Conflict of Interest

The authors declare no conflict of interest.

## Keywords

anisotropic property, lithium-ion batteries, Ni-rich layered oxides, radial arrangement

Received: December 24, 2018

Revised: January 26, 2019

Published online:

- [1] J. Lee, A. Urban, X. Li, D. Su, G. Hautier, G. Ceder, *Science* **2014**, 343, 519.  
 [2] W. Liu, P. Oh, X. Liu, M. J. Lee, W. Cho, S. Chae, Y. Kim, J. Cho, *Angew. Chem., Int. Ed.* **2015**, 54, 4440.  
 [3] F. Lin, D. Nordlund, Y. Li, M. K. Quan, L. Cheng, T.-C. Weng, Y. Liu, H. L. Xin, M. M. Doeff, *Nat. Energy* **2016**, 1, 15004.

- [4] Y. Su, G. Chen, L. Chen, W. Li, Q. Zhang, Z. Yang, Y. Lu, L. Bao, J. Tan, R. Chen, S. Chen, F. Wu, *ACS Appl. Mater. Interfaces* **2018**, 10, 6407.  
 [5] P. Yan, J. Zheng, J. Liu, B. Wang, X. Cheng, Y. Zhang, X. Sun, C. Wang, J.-G. Zhang, *Nat. Energy* **2018**, 3, 600.  
 [6] H.-H. Ryu, K.-J. Park, C. S. Yoon, Y.-K. Sun, *Chem. Mater.* **2018**, 30, 1155.  
 [7] G. Z. Wei, X. Lu, F. S. Ke, L. Huang, J. T. Li, Z. X. Wang, Z. Y. Zhou, S. G. Sun, *Adv. Mater.* **2010**, 22, 4364.  
 [8] A. O. Kondrakov, A. Schmidt, J. Xu, H. Geßwein, R. Mönig, P. Hartmann, H. Sommer, T. Brezesinski, J. Janek, *J. Phys. Chem. C* **2017**, 121, 3286.  
 [9] H. Kim, M. G. Kim, H. Y. Jeong, H. Nam, J. Cho, *Nano Lett.* **2015**, 15, 2111.  
 [10] J. Rana, S. Glatthaar, H. Gesswein, N. Sharma, J. R. Binder, R. Chernikov, G. Schumacher, J. Banhart, *J. Power Sources* **2014**, 255, 439.  
 [11] W. Li, U. H. Kim, A. Dolocan, Y. K. Sun, A. Manthiram, *ACS Nano* **2017**, 11, 5853.  
 [12] C. S. Yoon, K.-J. Park, U.-H. Kim, K. H. Kang, H.-H. Ryu, Y.-K. Sun, *Chem. Mater.* **2017**, 29, 10436.  
 [13] Y. Cho, P. Oh, J. Cho, *Nano Lett.* **2013**, 13, 1145.  
 [14] S.-H. Lee, C. S. Yoon, K. Amine, Y.-K. Sun, *J. Power Sources* **2013**, 234, 201.  
 [15] P. Hou, J. Yin, M. Ding, J. Huang, X. Xu, *Small* **2017**, 13, 1701802.  
 [16] S. Muto, K. Tatsumi, Y. Kojima, H. Oka, H. Kondo, K. Horibuchi, Y. Ukyo, *J. Power Sources* **2012**, 205, 449.  
 [17] F. Fu, G.-L. Xu, Q. Wang, Y.-P. Deng, X. Li, J.-T. Li, L. Huang, S.-G. Sun, *J. Mater. Chem. A* **2013**, 1, 3860.  
 [18] D. Luo, G. Li, C. Fu, J. Zheng, J. Fan, Q. Li, L. Li, *J. Power Sources* **2015**, 276, 238.  
 [19] E.-J. Lee, Z. Chen, H.-J. Noh, S. C. Nam, S. Kang, D. H. Kim, K. Amine, Y.-K. Sun, *Nano Lett.* **2014**, 14, 4873.  
 [20] B.-B. Lim, S.-T. Myung, C. S. Yoon, Y.-K. Sun, *ACS Energy Lett.* **2016**, 1, 283.  
 [21] W. Hua, W. Liu, M. Chen, S. Indris, Z. Zheng, X. Guo, M. Bruns, T.-H. Wu, Y. Chen, B. Zhong, S. Chou, Y.-M. Kang, H. Ehrenberg, *Electrochim. Acta* **2017**, 232, 123.  
 [22] T. Ohzuku, A. Ueda, M. Nagayama, Y. Iwakoshi, H. Komori, *Electrochim. Acta* **1993**, 38, 1159.  
 [23] W. Li, J. N. Reimers, J. R. Dahn, *Solid State Ionics* **1993**, 67, 123.  
 [24] J. Zhao, W. Zhang, A. Huq, S. T. Mixture, B. Zhang, S. Guo, L. Wu, Y. Zhu, Z. Chen, K. Amine, F. Pan, J. Bai, F. Wang, *Adv. Energy Mater.* **2017**, 7, 1601266.  
 [25] P. Yan, J. Zheng, M. Gu, J. Xiao, J.-G. Zhang, C.-M. Wang, *Nat. Commun.* **2017**, 8, 14101.  
 [26] B. Xiao, X. Sun, *Adv. Energy Mater.* **2018**, 8, 1802057.  
 [27] K.-J. Park, M.-J. Choi, F. Maglia, S.-J. Kim, K.-H. Kim, C. S. Yoon, Y.-K. Sun, *Adv. Energy Mater.* **2018**, 8, 1703612.  
 [28] F. Lin, D. Nordlund, I. M. Markus, T.-C. Weng, H. L. Xin, M. M. Doeff, *Energy Environ. Sci.* **2014**, 7, 3077.  
 [29] C. Tian, Y. Xu, D. Nordlund, F. Lin, J. Liu, Z. Sun, Y. Liu, M. Doeff, *Joule* **2018**, 2, 464.  
 [30] S.-T. Myung, K. Amine, Y.-K. Sun, *J. Mater. Chem.* **2010**, 20, 7074.  
 [31] X. He, C. Du, B. Shen, C. Chen, X. Xu, Y. Wang, P. Zuo, Y. Ma, X. Cheng, G. Yin, *Electrochim. Acta* **2017**, 236, 273.  
 [32] I. T. Kim, J. C. Knight, H. Celio, A. Manthiram, *J. Mater. Chem. A* **2014**, 2, 8696.  
 [33] W. Hua, J. Zhang, Z. Zheng, W. Liu, X. Peng, X. D. Guo, B. Zhong, Y. J. Wang, X. Wang, *Dalton Trans.* **2014**, 43, 14824.  
 [34] Y. H. Rho, K. Kanamura, *J. Electrochem. Soc.* **2004**, 151, A1406.